Manfred Wildner*, Martin Ende, Johannes M. Meusburger, Roland Kunit, Philipp Matzinger, Dominik Talla and Ronald Miletich

$CoSO_4 \cdot H_2O$ and its continuous transition compared to the compression properties of isostructural kieserite-type polymorphs

https://doi.org/10.1515/zkri-2021-2038
Received June 18, 2021; accepted August 10, 2021;
published online September 1, 2021

Abstract: The kieserite-type compound cobalt(II) sulfate monohydrate, $CoSO_4 \cdot H_2O$, has been investigated under isothermal (T = 295 K) hydrostatic compression up to 10.1 GPa in a diamond anvil cell by means of single-crystal X-ray diffraction and Raman spectroscopy. The monoclinic α-phase (space group $C2/c$) undergoes a second-order ferroelastic phase transition at P_c = 2.40(3) GPa to a triclinic β-phase (space group $P\bar{1}$). Lattice elasticities derived from fitting third-order Birch-Murnaghan equations of state to the pressure dependent unit-cell volume data yield V_0 = 354.20(6) Å^3, K_0 = 53.0(1.7) GPa, K' = 5.7(1.8) for the α-phase and V_0 = 355.9(8) Å^3, K_0 = 45.2(2.6) GPa, K' = 6.6(6) for the β-phase. Crystal structure data of the high-pressure polymorph were determined at 2.98(6) and 4.88(6) GPa. The most obvious structural feature and thus a possible driving mechanism of the phase transition, is a partial rearrangement in the hydrogen bonding system. However, a comparative analysis of pressure-induced changes in the four kieserite-type compounds investigated to date suggests that the loss of the point symmetry 2 at the otherwise rather rigid SO_4 tetrahedron, allowing symmetrically unrestricted tetrahedral rotations and edge tiltings in the β-phase, could be the actual driving mechanism of the phase transition.

Keywords: cobalt sulfate monohydrate; diamond-anvil cell; ferroelastic phase transition; high-pressure; kieserite-type compounds.

***Corresponding author: Manfred Wildner**, Department of Mineralogy and Crystallography, University of Vienna, Althanstraße 14, A-1090 Wien, Austria, E-mail: manfred.wildner@univie.ac.at
Martin Ende, Roland Kunit, Philipp Matzinger, Dominik Talla and Ronald Miletich, Department of Mineralogy and Crystallography, University of Vienna, Althanstraße 14, A-1090 Wien, Austria
Johannes M. Meusburger, Department of Mineralogy and Crystallography, University of Vienna, Althanstraße 14, A-1090 Wien, Austria; and Camborne School of Mines, University of Exeter, Penryn TR10 9FE, Cornwall, UK

1 Introduction

Hydrated sulfates and their properties have most recently gained increased interest after reports of extraterrestrial occurrences of individual representatives, for example on the surface of Mars or Jupiter's and Saturn's icy moons [1–10]. This includes the monoclinic kieserite-type monohydrate salts α-M(II)$SO_4 \cdot H_2O$ (space group $C2/c$) of Mg (i.e. kieserite) and divalent transition metal cations and their intermiscibility within continuous solid solution series [11–15]. Moreover, a special focus was placed on their behavior under astrophysically relevant conditions, such as corresponding to the temperature fluctuations on the surface or to elevated pressures at depths inside these planetary bodies [14–20].

Apart from a magnetic order-disorder transition reported for $FeSO_4 \cdot H_2O$ at 29.6 K [20], none of the M(II) $SO_4 \cdot H_2O$ compounds hitherto studied under variation of temperature reveal any temperature-induced structural phase transitions [14, 15]. At high pressures, however, endmember representatives with M(II) = Fe, Ni, and Mg display a ferroelastic phase transition under hydrostatic conditions [16–18]. The structural transformation is accompanied by a symmetry change from $C2/c$ to $P\bar{1}$ with a critical transition pressure occurring between 2.47 and 6.15 GPa. The mechanism of the phase transition shows all the properties of a typically continuous transformation, without any detectable volume discontinuity and without hysteresis with respect to the direction of transformation. From point of view of structural chemistry, a comparable, purely displacive mechanism for the transformation has been derived for the three representatives (i.e. $FeSO_4 \cdot H_2O$, $NiSO_4 \cdot H_2O$ and $MgSO_4 \cdot H_2O$) investigated so far. Without changing the actual polyhedral topology, the lattice distortion leads only to changes in the hydrogen bonding system, in which a shortened interpolyhedral O···O contact is included as acceptor, following the symmetry changes involved. For $NiSO_4 \cdot H_2O$ a second very subtle transition was discussed at higher but still hydrostatic pressure conditions and was explained from a crystallographic point of view by a disordered oxygen position,

which in turn leads to a further diversification of the existing hydrogen bonds.

For any systematic interpretation of the critical quantities, which are driving the actual transformation and which determine the relative stability criteria between the two polymorphs involved, too few crystallographic data have been available so far. In order to be able to assess the systematic relationships and influencing variables, the role of the different cations and their size, the cobalt representative $CoSO_4 \cdot H_2O$ and its high-pressure behavior have been determined in the course of this work.

2 Experimental

2.1 Synthesis of $CoSO_4 \cdot H_2O$

Sample crystals were grown under low hydrothermal conditions by a similar technique to that described earlier [12-15] at temperatures of around 483 K at autogenous H_2O vapor pressures in polytetrafluoroethylene-lined steel vessels. Euhedral crystals formed from a supersaturated aqueous solution of sulfuric acid (~0.4 ml concentrated H_2SO_4, Merck, ≥95%, CAS: 7664-93-9 + ~0.5 ml bidistilled H_2O) added to ~300 mg $CoSO_4 \cdot 7H_2O$ (Alfa Aesar™, 98%, CAS: 10026-24-1) inside the reaction chamber. After maintaining the inserted mixture at maximum T for ~270 h, it was cooled down to room temperature within 24 h in a non-linear fashion starting at a rate of around −1 K/min. The solid run products were separated from the remaining aqueous solution, washed with pure H_2O and ethanol and finally dried overnight at T = 353 K.

2.2 High-pressure sample environment

Selected crystals of $CoSO_4 \cdot H_2O$ were loaded into *ETH*-type [21] diamond-anvil cells (DAC) equipped with either standard brilliant-cut or Böhler Almax-type [22] type-I diamond anvils (culet diameter = 0.6 mm). Pressure chambers were prepared from stainless steel gaskets pre-indented to ~90–100 µm thickness with boreholes with 250 µm in diameter. 4:1 methanol–ethanol mixtures were used as pressure-transmitting medium for the X-ray diffraction investigations, while *in-situ* vibrational spectroscopy was carried out on crystals pressurized in cryogenically loaded argon. Pressures were determined using conventional quartz and ruby standards, applying calibration according to [23] and [24], respectively. The uncertainties in pressure obtained by the internal quartz standard were derived from the unit-cell volume data and their estimated standard deviations. Those obtained from the R_1-line shift of the ruby luminescence spectra have been estimated to be ±0.06 GPa after averaging repeated measurements.

2.3 *In-situ* Raman investigations

In-situ Raman spectra were collected from a 140 × 70 × 50 µm^3 sized $CoSO_4 \cdot H_2O$ crystal compressed in dense argon. Spectra were acquired by means of a confocal *Horiba Jobin Yvon LabRAM-HR 800* spectrometer using a red He–Ne laser source (operated at 20 mW power at a wavelength of 632.8 nm), an *Olympus BX41* microscope, a mercury-cadmium-telluride detector, and an *Olympus LMPlanFL N 50×* objective with a long working distance of 10.6 mm. A diffraction grating with 600 lines per mm was used for the measurements, and spectra were acquired using the software *LabSpec 6* (*HORIBA Scientific*) in the spectral range from 35 to 1190 cm^{-1} shift with an exposure time of 2 × 60 s. The recorded spectra were fitted with the Gauss-Lorentz-area method after background subtraction achieved using the program *Peakfit 4.1.2* (*Systat Software Inc.*).

2.4 Single-crystal X-ray diffraction

XRD Bragg peak positions were measured on a *Stoe AED II* diffractometer using a conventional scintillation counter, non-monochromatized Mo radiation, with the peak centering procedure being controlled through the *SINGLE* [25] software. For each pressure point, 16–23 individual Bragg reflections were measured in the 8-position centering mode [26]. Lattice parameters were refined in a first step without any symmetry constraints in order to identify changes in metrics and were finally constrained to monoclinic symmetry for the data points ≤2.40(3) GPa. The equations of state (EoS) were fitted by applying weighted least-square techniques using the software *EoSFit7* [27]. Normalized pressure-strain analyses were carried out in order to determine the relevant order of truncation of the Birch-Murnaghan (BM) EoS. Intensity data collections were performed on a bicrystal mount (crystal sizes: 230 × 30 × 30 µm^3 and 240 × 50 × 40 µm^3). The intensity data sets were measured on a *Stoe StadiVari* diffractometer using a *DECTRIS Pilatus 300K* detector with a 450 µm silicon layer and an air-cooled *Incoatec IµS* molybdenum high-brilliance micro-focus tube source (50 kV, 1 mA, beam size ≈ 110 µm). Frames were collected with angular steps of 0.5° in ω rotational mode with the χ circle fixed to a value ranging from 0° to 90°. Data were collected on both sides of the DAC as achieved by a 180° rotation of the φ circle after each run. The exposure time was set to 100 s per frame. Intensities were integrated using the *X-area 1.72* (*STOE & Cie GmbH*) software and corrected for absorption through the sample and DAC components by using the *ABSORB* [28] code. Initial positional parameters for the refinements were assigned according to those reported by [16]. Hydrogen positions were derived from difference-Fourier summation and refined with an isotropic displacement parameter U_{iso}, for the high-P data sets constrained to a value of 0.05 Å^2. All refinements were carried out using neutral scattering curves from the International Tables for Crystallography [29] using SHELXL [30] and the graphical user interface SHELXLE [31]. For data sets measured in the DAC, refinements were carried out with isotropic displacement parameters even for the oxygen atoms, while the 1-bar data were refined with anisotropic displacement parameters for all non-hydrogen atoms. For consistency it should be mentioned that the hydrogen bond donor atom here referred to as Ow corresponds to the O3 atom reported elsewhere [e.g. 11–15, 18, 20].

CSD 2099572–2099574 contain the supplementary crystallographic data for this paper. These data can be obtained free of charge from The Cambridge Crystallographic Data Centre via www.ccdc.cam.ac.uk/data_request/cif.

3 Results and discussion

3.1 Evidence of transformation in $CoSO_4 \cdot H_2O$ Raman spectra

In-situ high-pressure Raman spectra have been collected in a sequence of 24 individual spectra in total, recorded between 0.4 and 10.1 GPa (Figure 1). All spectra were acquired in the Raman shift range 35–1190 cm^{-1}, while any attempt to measure the vibration response related to the molecular H_2O in the range 2600–3500 cm^{-1} failed due to high background luminescence. The observed band positions and intensities match those reported for isostructural $NiSO_4 \cdot H_2O$ [18], $MgSO_4 \cdot H_2O$ [17], and $FeSO_4 \cdot H_2O$ [16], and can be assigned following [15]. The typical blueshifts on increasing pressure correspond to rates between 1.52(4) and 7.62(7) cm^{-1}/GPa for the bands at 1027.2(2) and 279.0(5) cm^{-1}, respectively.

As with the other isostructural representatives, the appearance of the bands and their pressure dependencies in $CoSO_4 \cdot H_2O$ do not necessarily reveal a transformation immediately. This finding once again indicates that the changes in the crystal structure are only very subtle and do not involve a change in coordination or any comparable change related to the bonding topology. Only on closer inspection, one recognizes for several bands that the quasi-linear shift slightly changes its slope at around 2.4 GPa, with different $d\tilde{\nu}/dP$ values before and after the presumable critical pressure (Figure 1). This observation was also made earlier with the isotypic compounds, where evidence for potential transformations has also been attributed exclusively to the change in the $d\tilde{\nu}/dP$ slopes. The lack of band splitting also applies to $CoSO_4 \cdot H_2O$, which can be attributed to the fact that the point symmetries of the most prominent functional groups remain largely unchanged across the transformation itself. A splitting of the prominent $\tilde{\nu}_1(SO_4)$ stretching mode as described for the Ni representative, forming a shoulder on the low-frequency side of this band, could not be observed. Hence, a further transformation, inferable from such diagnostic features, was not detected in $CoSO_4 \cdot H_2O$ within the investigated pressure range.

3.2 Lattice properties and static elasticity of $CoSO_4 \cdot H_2O$

The lattice properties, on the other hand, show a completely different picture with evident changes that clearly reveal a triclinic distortion of the originally monoclinic structure

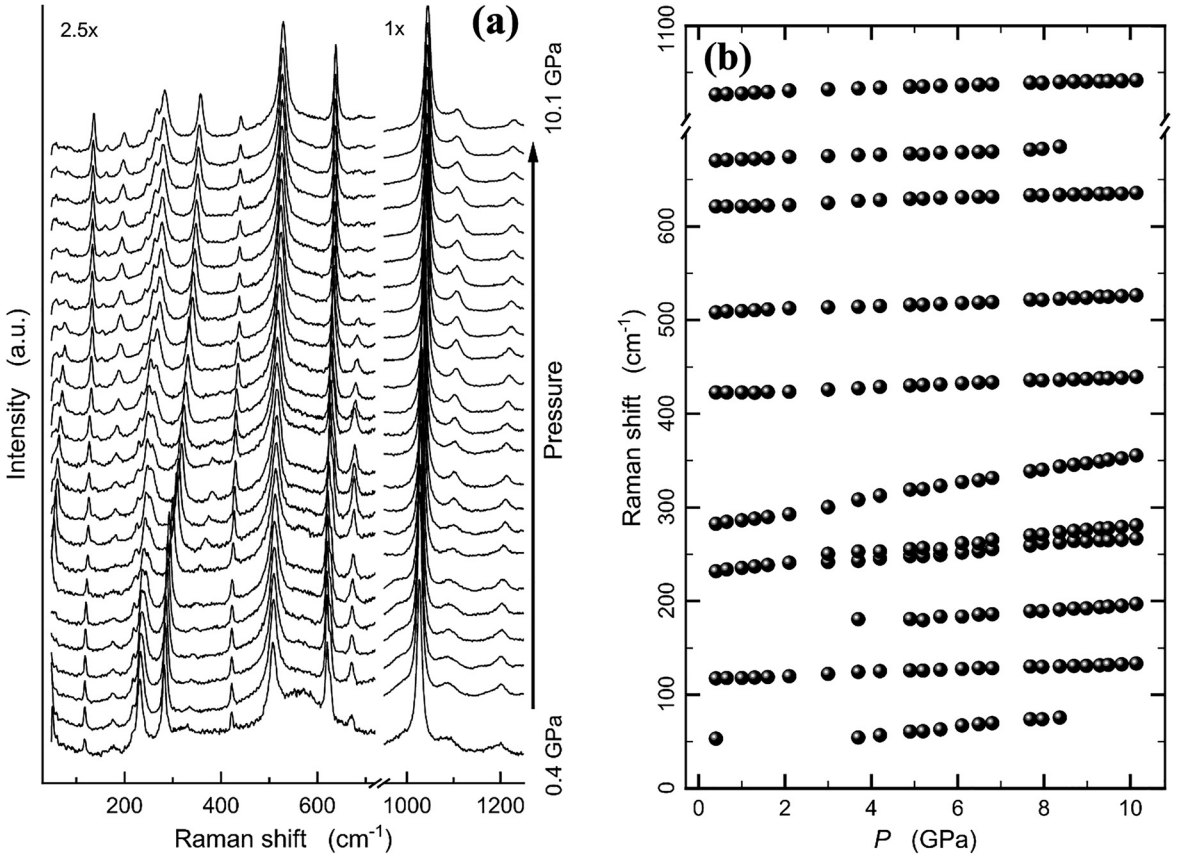

Figure 1: *In-situ* high-pressure Raman spectra of $CoSO_4 \cdot H_2O$ recorded between 0.4 and 10.1 GPa (a), and their pressure dependence (b).

(Table 1, Figure 2). Precise lattice parameters and the unit-cell volume were measured at 32 pressure points under hydrostatic conditions between 0.51 and 8.94 GPa. Both the base vector lengths a, b and c but also the deviations from angles set for the monoclinic system suggest the onset of transformation between 2.40 and 2.63 GPa. The adherence to identical parameters within the reduced cell (i.e. $a_{red} = b_{red}$, $\alpha_{red} = \beta_{red}$) in the monoclinic low-pressure phase, compared to the apparent diversification of these values at higher pressures, clearly proves the triclinic distortion (Table 1, Figure 2). The fashion of distortion is absolutely equivalent to what has been reported for the other kieserite-type monohydrates [16-18]. Moreover, the calculated spontaneous strain matches the previously reported evolution of strain tensor components and their eigenvalues. A fit of the lattice angle γ follows the power-

Table 1: Lattice parameters and unit-cell volumes of $CoSO_4 \cdot H_2O$ determined at static pressures between 10^{-4} and 8.94(2) GPa. The lattice parameters at non-ambient pressures correspond to unconstrained refinements according to the setting of the reduced cell ($Z = 2$).

P (GPa)	a (Å)	b (Å)	c (Å)	α (°)	β (°)	γ (°)	V (Å^3)
0.0001[a]	6.9641(5)	7.5931(7)	7.6261(9)	90.003(9)	118.560(6)	89.999(7)	354.19(6)
0.507(9)	5.1392(5)	5.1405(6)	7.5900(17)	108.899(12)	108.874(10)	94.804(8)	175.47(4)
	6.9574(7)	*7.5662(5)*	*7.5892(12)*	*90*	*118.565(6)*	*90*	*350.87(6)*
0.840(18)	5.1311(6)	5.1329(6)	7.5668(17)	108.909(12)	108.904(12)	94.719(9)	174.42(4)
	6.9515(7)	*7.5497(6)*	*7.5674(13)*	*90*	*118.562(7)*	*90*	*348.82(6)*
1.173(18)	5.1237(5)	5.1256(6)	7.5445(17)	108.921(12)	108.914(11)	94.643(8)	173.44(4)
	6.9466(7)	*7.5343(5)*	*7.5450(13)*	*90*	*118.558(7)*	*90*	*346.84(6)*
1.584(18)	5.1152(5)	5.1168(6)	7.5183(18)	108.935(12)	108.922(12)	94.564(9)	172.28(5)
	6.9403(7)	*7.5167(6)*	*7.5185(14)*	*90*	*118.556(7)*	*90*	*344.51(6)*
1.890(18)	5.1087(5)	5.1107(6)	7.4983(16)	108.948(12)	108.914(10)	94.514(8)	171.43(4)
	6.9353(7)	*7.5038(6)*	*7.4977(13)*	*90*	*118.546(7)*	*90*	*342.75(6)*
2.166(18)	5.1030(7)	5.1052(6)	7.4817(17)	108.956(12)	108.918(14)	94.465(11)	170.69(4)
	6.9307(8)	*7.4924(6)*	*7.4810(15)*	*90*	*118.539(8)*	*90*	*341.26(7)*
2.399(33)	5.0994(7)	5.1003(8)	7.4686(19)	108.973(14)	108.916(15)	94.422(11)	170.12(5)
	6.9292(9)	*7.4836(7)*	*7.4665(16)*	*90*	*118.553(8)*	*90*	*340.08(7)*
2.634(33)	5.1107(12)	5.0738(21)	7.4545(28)	109.075(36)	108.762(27)	94.408(24)	169.37(9)
2.881(33)	5.1128(5)	5.0629(10)	7.4408(16)	109.165(16)	108.797(11)	94.304(10)	168.67(4)
3.102(24)	5.1134(9)	5.0531(8)	7.4288(15)	109.214(14)	108.785(19)	94.253(14)	168.08(4)
3.391(69)	5.1128(10)	5.0421(11)	7.4128(16)	109.264(18)	108.761(21)	94.205(16)	167.34(5)
3.742(39)	5.1115(11)	5.0289(10)	7.3929(16)	109.309(18)	108.741(24)	94.154(19)	166.41(5)
4.107(24)	5.1097(7)	5.0173(8)	7.3741(12)	109.344(13)	108.726(15)	94.116(12)	165.55(4)
4.342(15)	5.1088(4)	5.0111(7)	7.3646(10)	109.372(13)	108.730(10)	94.080(9)	165.08(3)
4.803(15)	5.1061(4)	4.9972(7)	7.3428(10)	109.398(13)	108.707(10)	94.048(9)	164.07(3)
5.201(24)	5.1034(4)	4.9863(6)	7.3235(10)	109.420(11)	108.683(10)	94.024(8)	163.21(3)
5.433(24)	5.1016(5)	4.9801(8)	7.3114(11)	109.433(13)	108.685(11)	94.000(10)	162.67(3)
5.863(15)	5.0988(4)	4.9689(8)	7.2932(11)	109.441(14)	108.686(10)	93.974(9)	161.82(3)
6.066(21)	5.0967(4)	4.9638(8)	7.2827(11)	109.452(13)	108.673(10)	93.960(9)	161.37(3)
6.264(21)	5.0941(5)	4.9587(7)	7.2753(12)	109.459(13)	108.685(12)	93.941(10)	160.99(4)
6.582(30)	5.0930(6)	4.9512(6)	7.2612(11)	109.468(11)	108.680(13)	93.921(10)	160.37(3)
6.826(27)	5.0915(6)	4.9455(5)	7.2507(11)	109.476(10)	108.676(14)	93.910(10)	159.90(3)
6.959(24)	5.0909(6)	4.9422(5)	7.2460(11)	109.475(10)	108.678(14)	93.908(10)	159.67(3)
7.241(18)	5.0890(6)	4.9359(5)	7.2351(12)	109.474(10)	108.658(14)	93.908(10)	159.20(3)
7.399(24)	5.0879(6)	4.9321(5)	7.2278(12)	109.472(10)	108.661(14)	93.905(10)	158.88(3)
7.670(24)	5.0861(5)	4.9262(6)	7.2157(14)	109.469(11)	108.642(12)	93.912(10)	158.39(3)
7.924(15)	5.0847(5)	4.9205(5)	7.2060(15)	109.465(11)	108.631(11)	93.919(8)	157.96(4)
8.246(27)	5.0833(6)	4.9137(7)	7.1948(16)	109.475(13)	108.642(14)	93.897(11)	157.44(4)
8.408(36)	5.0823(5)	4.9094(7)	7.1892(16)	109.470(13)	108.653(12)	93.887(10)	157.16(4)
8.668(39)	5.0819(11)	4.9050(18)	7.1801(32)	109.469(33)	108.654(25)	93.897(22)	156.79(9)
8.649(21)	5.0815(4)	4.9049(7)	7.1794(17)	109.467(13)	108.650(10)	93.894(8)	156.77(4)
8.941(21)	5.0800(9)	4.8990(12)	7.1685(19)	109.481(22)	108.653(19)	93.882(17)	156.29(6)

[a]Unconstrained refinement in $C2/c$ setting of a different crystal on a micro mount holder at ambient conditions. For monoclinic α-$CoSO_4 \cdot H_2O$ ($P \leq 2.40(3)$ GPa), the results of constrained refinements according to the $C2/c$ setting ($Z = 4$) are given in a second line in italics.

law function with a critical exponent β being close to the ideal value of 0.5 as typical for a second-order phase transition.

Fitting the values for the unit-cell volumes and the base vectors in superordinate $C2/c$ setting (Figure 2) to parametrized equations of state (EoS), the resulting moduli, i.e. the bulk modulus K and the axial moduli M_i and their pressure derivatives, match very well with those for the other isostructural kieserite-type representatives (Table 2). The EoS fits for the low-P polymorph α-$CoSO_4{\cdot}H_2O$ are limited to a relatively narrow pressure range between 10^{-4} and 2.4 GPa and are restricted to 8 data points. A fit according to a third-order Birch-Murnaghan (BM-3) formalism [32] yields $K_0 = 53.0 \pm 1.7$ GPa with $dK/dP = 5.7 \pm 1.8$, which fits into the series of values being greater than 4, thus confirming equivalent compression behavior for the $C2/c$ α-form of the kieserite-type compounds. The re-evaluation of the volume data of α-$NiSO_4{\cdot}H_2O$ shows 65.9 ± 6.7 GPa with $dK/dP = 2.3 \pm 4.6$ for an unconstrained equivalent BM-3 fit, whereas it yields 60.1 ± 1.0 GPa for dK/dP set to 6.5. The unconstrained fit to the data of α-$MgSO_4{\cdot}H_2O$ provides $K_0 = 48.1 \pm 0.5$ GPa with $dK/dP = 8.1 \pm 0.6$. The comparable values obtained in this way also correspond to the Anderson–Anderson relationship [33], with indirectly proportional relationships between the volume compressibility and the molar volume within an isostructural series. Even if the absolute numbers for the individual crystallographic directions are subject to somewhat greater fluctuations, a comparable behavior is also proven for the compressional anisotropy. The a-axis is the stiffest, while along the

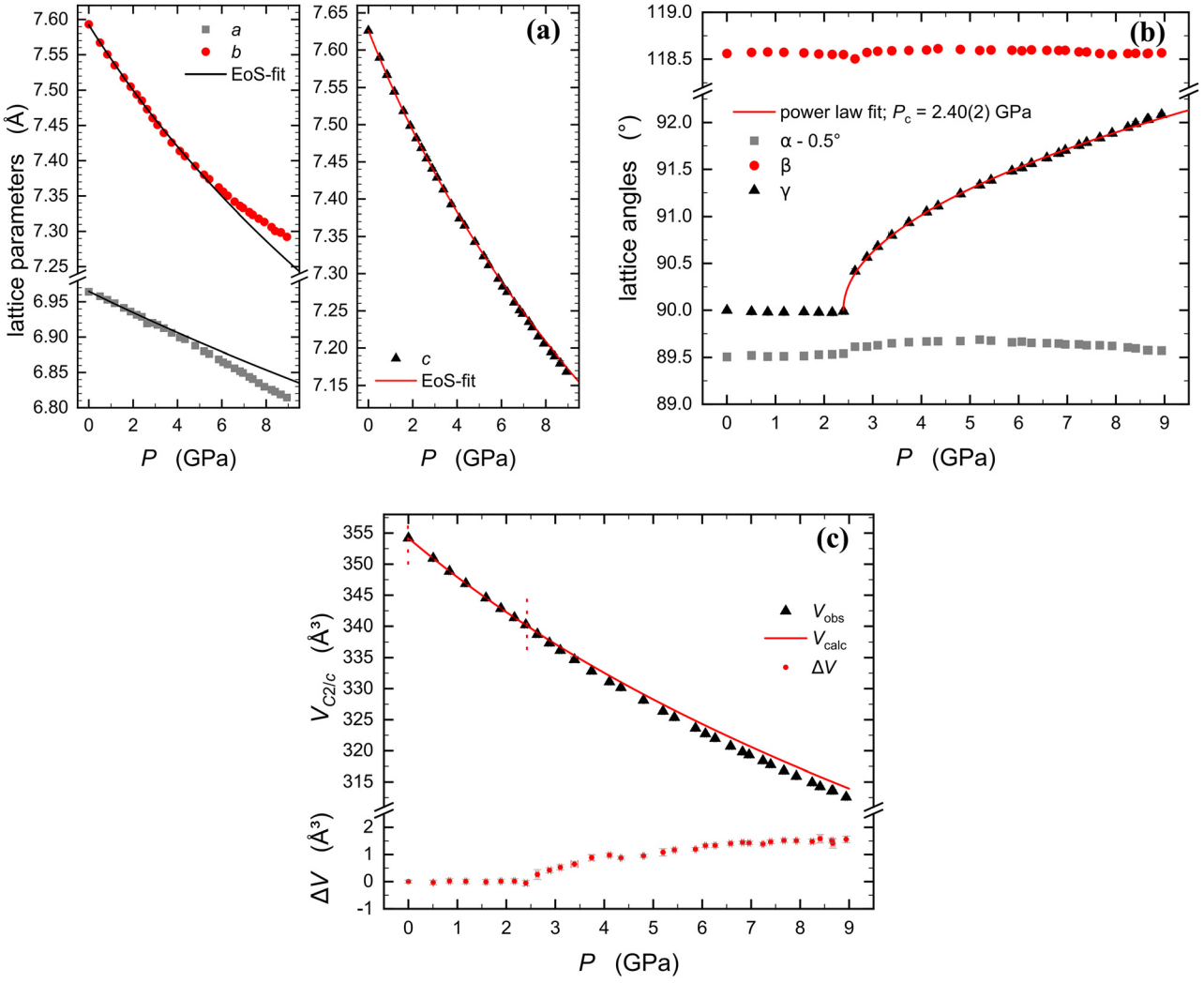

Figure 2: Pressure evolution of the unit-cell parameters of $CoSO_4{\cdot}H_2O$ between 10^{-4} and 8.94 GPa, referring to the monoclinic $C2/c$ cell setting of the α-phase: (a) lattice parameter a, b, and c; (b) angles α, β, and γ; (c) cell volume V. Solid lines correspond to fits and their extrapolations beyond or below P_c, respectively, following equations of state (EoS-fit) or a power-law equation.

directions of the crystallographic *b*- and *c*-axes the compressibilities are more or less similar for each of the four representatives (Table 2).

The elastic properties of the lattice of the high-pressure polymorph (β-$CoSO_4 \cdot H_2O$) offer a similar picture, both in terms of volume compressibility and anisotropy (Table 2). It is noteworthy that dK/dP for the β-phase of all representatives is much closer to the value $K' = 4$. Moreover, the anisotropy is once again similar, and more or less the same in comparison to the α-phase, which is not surprising, since the two structures have identical bond topologies with different symmetries. The high-pressure range beyond 7 GPa deserves special attention, since subtle deviations from linear developments have been seen as an indication of the existence of a further phase, namely the γ-form of the Ni(II)-kieserite analogue [18], comprising a disordered O2B hydrogen bond acceptor position (cf. Figure 3) and hence a further diversified hydrogen bonding system. Despite all the similarities that are evident in many respects, especially between the Co(II) and Ni(II) analogue phases, a comparably significant deviation could not be observed. As a result from the findings in this study, we refrain from postulating the existence of an equivalent γ-$CoSO_4 \cdot H_2O$ polymorph within the investigated pressure range.

3.3 Crystal structure of the β-$CoSO_4 \cdot H_2O$ polymorph

In-situ high-pressure crystal structure investigations on $CoSO_4 \cdot H_2O$ were performed at 3.0 and 4.9 GPa from a bicrystal mount in a DAC, in addition to single-crystal data collection at ambient pressure from a sample mounted on a glass fibre. While the 1-bar structure was refined in $C2/c$ according to [12] (matching the recent refinement by [13] very closely), all high-pressure crystal structures were refined in $P\bar{1}$ in the setting of the reduced cell according to [16–18]. The final refinements confirm the space-group symmetries, which have also been reported earlier for the analogue phases and polymorphs of Mg(II), Fe(II) and Ni(II). Details of the intensity data collections and the results of refinements are summarized in Table 3, the resulting positional parameters and refined displacement parameters are listed in Table 4, and selected interatomic distances are summarized in Table 5. Selected sections of the crystal structures of α- and β-$CoSO_4 \cdot H_2O$ are compared in Figure 3.

While the S atoms occupy a single position in both space groups, the Co atoms are located on two individual sites (i.e. CoA and CoB) in $P\bar{1}$. The same applies to the O1 and O2 sites, which both split into two independent sites (O1A, O1B, and O2A, O2B), while the Ow position maintains a single site both in $C2/c$ and $P\bar{1}$. The sulfate tetrahedron loses its former point symmetry 2 in the triclinic high-pressure polymorph.

The SO_4 group behaves as rather rigid unit over the full investigated pressure range, whereas mean Co–O distances and volumes of both $Co(A/B)O_6$ octahedra steadily decrease with pressure, albeit in a somewhat different way for the A and B site in the high-P polymorph (Table 5, see also next section). As the kieserite-type structure topology remains the same across the phase transition, the structure accommodates increasing densification by mutual polyhedral tiltings and rotations. The bond angles at the

Table 2: Equation of state parameters of the unit-cell volumes V and the crystallographic base vectors a, b, and c for various kieserite-type polymorphs. Elastic moduli K and M and their pressure derivatives K' and M' were obtained from fitting Birch-Murnaghan equations to experimental data for α-M(II)$SO_4 \cdot H_2O$ and β-M(II)$SO_4 \cdot H_2O$.

Phase (M)	α-Co[a]	β-Co[a]	α-Ni [18]	β-Ni [18]	α-Mg [17]	β-Mg [17]	α-Fe [16]	β-Fe [16]
V_0 (Å^3)	354.2(1)	355.9(8)[b]	342.3(1)	342.1(6)[b]	355.5(4)	355.8(1.8)[b]	365.2(3)	367.0(4)[b]
a_0 (Å)	6.965(1)	6.984(1)[b]	6.826(1)	6.838(4)[b]	6.909(1)	6.911(1)[b]	7.082(1)	7.087(4)[b]
b_0 (Å)	7.592(1)	7.552(4)[b]	7.598(1)	7.576(6)[b]	7.628(1)	7.649(1)[b]	7.553(1)	7.54(1)[b]
c_0 (Å)	7.626(1)	7.626(7)[b]	7.403(1)	7.414(6)[b]	7.642(1)	7.615(14)[b]	7.779(1)	7.784(4)[b]
K_0 (GPa)	53.0(1.7)	45.2(2.6)	60.1(1.0)[c]	61.3(1.9)[d]	48.1(5)	49.3(5.5)	45.2(2)	45.1(6)
K'	5.7(1.8)	6.6(6)	6.5[e]	4.0[e]	8.1(6)	4.8(1.0)	6.7(1)	5.4[e]
M_a (GPa)	451(11)	316(4)	401(12)	332(16)	297(12)	383(27)	496(9)	471(19)
M_a'	12[e]	12[e]	12[e]	12[e]	21(14)	−6(2)	1.3(3.2)	3.0[e]
M_b (GPa)	152(2)	201(4)	175(4)	191(7)	142(4)	83.5(5.5)	109(2)	112(7)
M_b'	12[e]	12[e]	12[e]	12[e]	30(5)	45.9(5.5)	36(2)	36.8[e]
M_c (GPa)	101.3(1.1)	102(5)	200(4)	169(6)	94.1(1.3)	122(11)	93.8(7)	102(1)
M_c'	12[e]	11.2(9)	12[e]	12[e]	15.1(1.4)	8.0(1.5)	13.1(4)	9.1[e]

[a]This study. [b]Theoretical values extrapolated back to $P = 1$ bar. [c]Re-evaluated after fitting a BM-3 EoS with constrained K' value. [d]Fitted to BM-2 EoS (i.e. $K' = 4$ for volume data). [e]Constrained to this value for refinement.

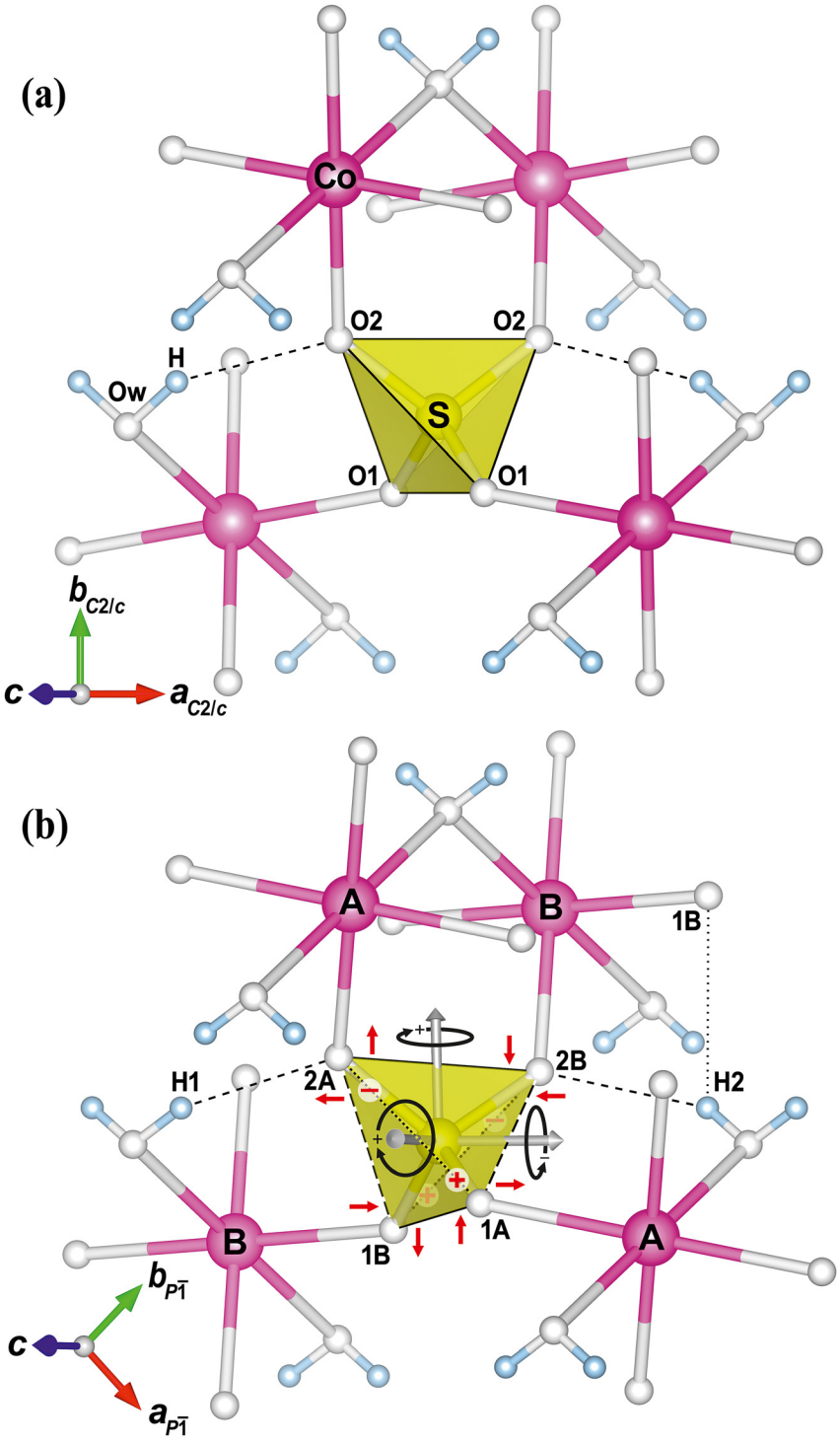

Figure 3: Selected sections of the crystal structures of (a) α-$CoSO_4{\cdot}H_2O$ (at 10^{-4} GPa) and (b) β-$CoSO_4{\cdot}H_2O$ (at 4.9 GPa) in projections down the approximate c^* direction (i.e. along [2 0 3]). For the β-phase, the direction of tetrahedral rotations (black arrows) and sense of edge tiltings (red arrows and +: up, –: down) relative to the α-phase are indicated, and tetrahedral edge line types correspond to those used in Figure 5(b).

bridging oxygen atoms (O1 and O2 both linking an octahedron with a tetrahedron, and the water molecule with Ow providing the link within the octahedral chains) undergo significant changes to generally smaller values, thus substantially reducing the volume of interpolyhedral voids. This results, as the most striking feature, in a partial modification of the hydrogen bonding scheme: In the monoclinic α-form, two symmetrically equivalent Ow–H···O2 hydrogen bonds (Figure 3(a)) of moderate strength (O···O = 2.72 Å; compare [34], where 2.805 and 2.546 Å are

Table 3: Crystal data and details of the intensity data collections and structure refinements for $CoSO_4 \cdot H_2O$ at 10^{-4}, 2.98 and 4.88 GPa.

Phase Pressure (GPa)	α-$CoSO_4 \cdot H_2O$ 10^{-4}	β-$CoSO_4 \cdot H_2O$ 2.98(6)	β-$CoSO_4 \cdot H_2O$ 4.88(6)
Space group	$C2/c$	$P\bar{1}$	$P\bar{1}$
a (Å)	6.9641(5)	5.0585(27)	4.9951(17)
b (Å)	7.5931(7)	5.1131(16)	5.1056(11)
c (Å)	7.6261(9)	7.4354(33)	7.3391(29)
α (°)	90	108.792(16)	108.702(17)
β (°)	118.560(6)	109.190(16)	109.402(17)
γ (°)	90	94.279(15)	94.043(13)
V (Å^3)	354.19	168.41	163.90
Z	4	2	2
Reflections with $F_o > 0\sigma(F_o)$	3108	6780	6833
Unique reflections with $F_o > 4\sigma(F_o)$	985	499	503
Unique reflections	1041	602	615
$2\theta_{max}$	79.38	73.10	74.03
h_{min}, h_{max}	−8, 12	−8, 8	−8, 8
k_{min}, k_{max}	−13, 13	−6, 6	−6, 6
l_{min}, l_{max}	−13, 13	−12, 11	−12, 11
R_{int}, R_{sigma}	0.0268, 0.018	−, 0.039	−, 0.054
R_1 for $F_o > 4\sigma(F_o)$	0.0151	0.0331	0.0383
w$R2$	0.0406	0.0863	0.0918
GooF	1.081	1.079	1.087
Number of refined parameters	40	50	50

given as respective average and shortest values for water molecules) contribute to the linkage between adjacent octahedral chains; in the triclinic β-phase, an additional weaker Ow–H2···O1B bond (2.94 Å at 4.88 GPa) is formed and a minor diversification of the further strengthened Ow–H(1/2)···O2 (A/B) bonds occurs (Table 5, Figure 3(b)). This rearrangement was also assumed to be a major driving force for the pressure-induced α- to β-transformation in other kieserite-type compounds [16–18].

3.4 Comparative high-pressure stereochemistry of M(II)$SO_4 \cdot H_2O$ phases

Figures 4 and 5 show selected crystal chemical and topological features of the M(II)$SO_4 \cdot H_2O$ compounds with respect to variations of their octahedral ionic radii [35] (Mg: 0.720, Fe: 0.780, Co: 0.745, and Ni: 0.690 Å). Apart from detailed differences discussed in the following, the Fe-compound shows an eye-catching deviation by the fact that its α- to β-transformation occurs at significantly higher pressures (P_c = 6.15 GPa) compared to the narrow range of moderate P_c values found for the other representatives (2.72, 2.40, and 2.47 GPa for M = Mg, Co, and Ni, respectively). Nevertheless, $FeSO_4 \cdot H_2O$ follows the same overall trends within this series of isostructural compounds. Figure 4(a) and (b) show the changes in the individual M–O bond lengths (a) and relative octahedral volumes (b) with pressure, yielding some remarkable features. The MgO_6 octahedra (both A and B) show the highest relative compressibilities, despite the comparatively small ionic radius and short ambient <Mg–O> of 2.078 Å [13], even exceeding the compressibility of the clearly larger FeO_6 octahedra. The polyhedral modulus K_{oct} of the Mg octahedra is only ~65–70 GPa, which corresponds to a compressibility approximately twice as large compared to the values usually found for MgO_6 in any oxide and silicate (~150 GPa [36]). On the other hand, the smallest octahedron around Ni exhibits, as expected, the highest stiffness within this group. The polyhedral connectivity through shared corners and the presence of H_2O ligands explains the generally high octahedral as well as bulk volume compressibilities of this structure type. In cases where the compressibilities of A and B octahedra differ significantly and consistently (i.e. Mg and Ni), the B octahedron is the more compressible one. For all four compounds, the octahedral bond length distortions decrease more or less in a similar fashion, with the respective angular distortions increasing steadily (Figure 4(c)).

A closer look at the individual M–O distances in Figure 4(a) reveals that the longest bonds to the Ow water molecules shorten the strongest, whereas the M–O1 bonds, oriented roughly along the monoclinc a-axis, are the stiffest ones, thus contributing to the observed high respective axial moduli M_a (Table 2). As illustrated in Figure 4(d), these differences also change the type of octahedral distortion with increasing pressure from a clearly elongated [4+2]-coordination (with a tendency towards [2+2+2] in $FeSO_4 \cdot H_2O$, as discussed by [14]) to a rather regular proper [6]-fold coordination for the A-octahedra of Co and Ni, and to even a [2+4]-type for Fe(A), whereas the B-octahedra tend to keep the former shape within the α-phases. However, only the MgO octahedra both maintain the distinct [4+2]-elongation present at ambient conditions.

In contrast, the sulfate tetrahedron behaves as a rather rigid unit within limits of error in all four compounds and over the full pressure ranges investigated. A tendency from the expected overall mean <S–O> bond length of 1.473 Å [37] at ambient pressures towards marginally smaller values with pressure is hardly significant (especially considering that the ambient data were obtained without

Table 4: Refined positional parameters and displacement parameters (Å^2) for (a) α-$CoSO_4 \cdot H_2O$ ($C2/c$) at 10^{-4} GPa, and β-$CoSO_4 \cdot H_2O$ ($P\bar{1}$) at (b) 2.98(6) and (c) 4.88(6) GPa.

(a)

Atom	Wyck.	x	y	z	U_{eq}
Co	4*b*	0	1/2	0	0.00809(5)
S	4*e*	0	0.15371(3)	1/4	0.00720(6)
O1	8*f*	0.17251(9)	0.04253(9)	0.40003(10)	0.01434(11)
O2	8*f*	0.09676(9)	0.26653(7)	0.15397(9)	0.01242(10)
Ow	4*e*	0	0.63861(10)	1/4	0.01112(12)
H	8*f*	0.105(3)	0.703(2)	0.292(3)	0.030(4)

	U_{11}	U_{22}	U_{33}	U_{23}	U_{13}	U_{12}
Co	0.00724(7)	0.00861(6)	0.00871(7)	0.00047(3)	0.00405(5)	−0.00007(3)
S	0.00556(9)	0.00728(8)	0.00886(9)	0	0.00353(7)	0
O1	0.0086(2)	0.0164(2)	0.0169(3)	0.0076(2)	0.0053(2)	0.0040(2)
O2	0.0123(2)	0.0114(2)	0.0168(2)	0.0048(2)	0.0097(2)	0.0018(2)
Ow	0.0109(3)	0.0124(3)	0.0108(3)	0	0.0059(2)	0

(b)

Atom	Wyck.	x	y	z	U_{eq}
Co1A	1*a*	0	0	0	0.0085(3)
Co1B	1*b*	0	0	1/2	0.0083(3)
S	2*i*	0.3470(3)	0.6458(3)	0.7533(5)	0.0076(4)
O1A	2*i*	0.6279(9)	0.7215(11)	0.9183(9)	0.0139(9)
O1B	2*i*	0.6967(9)	0.6417(10)	0.3917(8)	0.0122(9)
O2A	2*i*	0.1181(8)	0.6583(10)	0.8386(8)	0.0110(9)
O2B	2*i*	0.3287(8)	0.8462(11)	0.6464(8)	0.0118(9)
Ow	2*i*	0.8532(10)	0.1372(11)	0.7485(11)	0.0113(9)
H1	2*i*	0.89(3)	0.25(3)	0.78(3)	0.05[a]
H2	2*i*	0.68(2)	0.10(3)	0.70(2)	0.05[a]

	U_{11}	U_{22}	U_{33}	U_{23}	U_{13}	U_{12}
Co1A	0.0087(5)	0.0085(8)	0.0079(10)	0.0023(8)	0.0034(6)	0.0014(4)
Co1B	0.0077(5)	0.0089(8)	0.0073(9)	0.0020(8)	0.0026(5)	0.0013(4)
S	0.0071(6)	0.0081(10)	0.0056(12)	0.0001(10)	0.0023(7)	0.0004(5)

(c)

Atom	Wyck.	x	y	z	U_{eq}
Co1A	1*a*	0	0	0	0.0091(4)
Co1B	1*b*	0	0	1/2	0.0089(4)
S	2*i*	0.3456(3)	0.6407(4)	0.7558(3)	0.0079(4)
O1A	2*i*	0.6234(9)	0.7283(11)	0.9300(9)	0.0140(10)
O1B	2*i*	0.6839(9)	0.6493(10)	0.3816(8)	0.0106(9)
O2A	2*i*	0.1042(9)	0.6504(10)	0.8326(8)	0.0103(9)
O2B	2*i*	0.3256(9)	0.8321(12)	0.6392(9)	0.0133(10)
Ow	2*i*	0.8497(10)	0.1349(12)	0.7496(10)	0.0114(9)
H1	2*i*	0.90(2)	0.29(3)	0.78(2)	0.05[a]
H2	2*i*	0.70(2)	0.10(3)	0.71(2)	0.05[a]

	U_{11}	U_{22}	U_{33}	U_{23}	U_{13}	U_{12}
Co1A	0.0094(5)	0.0086(9)	0.0082(10)	0.0022(8)	0.0029(6)	0.0016(4)
Co1B	0.0080(5)	0.0092(9)	0.0080(9)	0.0023(8)	0.0020(5)	0.0013(4)
S	0.0077(6)	0.0072(11)	0.0072(12)	0.0012(10)	0.0023(6)	0.0011(5)

[a]Not refined.

Table 5: Selected interatomic distances (Å) in $CoSO_4 \cdot H_2O$ at 10^{-4}, 2.98 and 4.88 GPa.

	α-$CoSO_4 \cdot H_2O$ $P = 10^{-4}$ GPa		β-$CoSO_4 \cdot H_2O$ $P = 2.98(6)$ GPa	β-$CoSO_4 \cdot H_2O$ $P = 4.88(6)$ GPa
Co–O2	2.0540(6) 2×	CoA–O2A	2.031(4) 2×	2.029(4) 2×
Co–O1	2.0554(6) 2×	CoA–O1A	2.057(5) 2×	2.064(5) 2×
Co–Ow	2.1777(4) 2×	CoA–Ow	2.133(8) 2×	2.093(8) 2×
<Co–O>	2.096	<CoA–O>	2.074	2.062
		CoB–O2B	2.031(5) 2×	2.020(6) 2×
		CoB–O1B	2.043(4) 2×	2.036(4) 2×
		CoB–Ow	2.145(6) 2×	2.138(6) 2×
		<CoB–O>	2.073	2.065
S–O1	1.4665(6) 2×	S–O1A	1.463(5)	1.458(5)
		S–O1B	1.465(5)	1.464(5)
S–O2	1.4819(5) 2×	S–O2A	1.488(5)	1.489(5)
		S–O2B	1.476(7)	1.480(7)
<S–O>	1.474	<S–O>	1.473	1.473
Ow···O1	3.2931(10) 2×	Ow···O1A	3.293(7)	3.334(7)
		Ow···O1B	3.070(7)	2.939(8)
Ow···O2	2.7202 (6) 2×	Ow···O2A	2.659(8)	2.627(8)
		Ow···O2B	2.681(7)	2.668(7)

the DAC), neither in the four kieserites nor in limited data on high-pressure single crystal structure investigations on sulfates from the literature; e.g. for kainite, $KMg(SO_4)Cl \cdot 3H_2O$ [38], a reduction by only 1% within ~12 GPa was found, and in gypsum [39], $Ca(SO_4) \cdot 2H_2O$, as well as in blödite [40], $Na_2Mg(SO_4)_2 \cdot 4H_2O$, the <S–O> distances remain almost unchanged up to 4 and 10 GPa, respectively.

In spite of its incompressibility, the SO_4 group plays an important role for the structural changes in the kieserite-type compounds with pressure. On the one hand, inter-polyhedral *M*–O–S angles at the linking oxygen atoms O1 and O2 decrease with pressure (Figure 5(a)). This also applies to the octahedral chain angle *M*–Ow–*M*, indicating enhanced tilting and folding to reduce the interpolyhedral voids with increasing pressure. While the angles at Ow and O1(A/B) continue this trend across the phase transition, there is a strong differentiation between O2A versus O2B in the β-phases. Here it has to be mentioned that also under pressure these angles remain larger in the Mg phase compared to the other *M*(II) representatives, which has been attributed by [13] to the respective absence or presence of partly filled 3*d* orbitals and related differences in

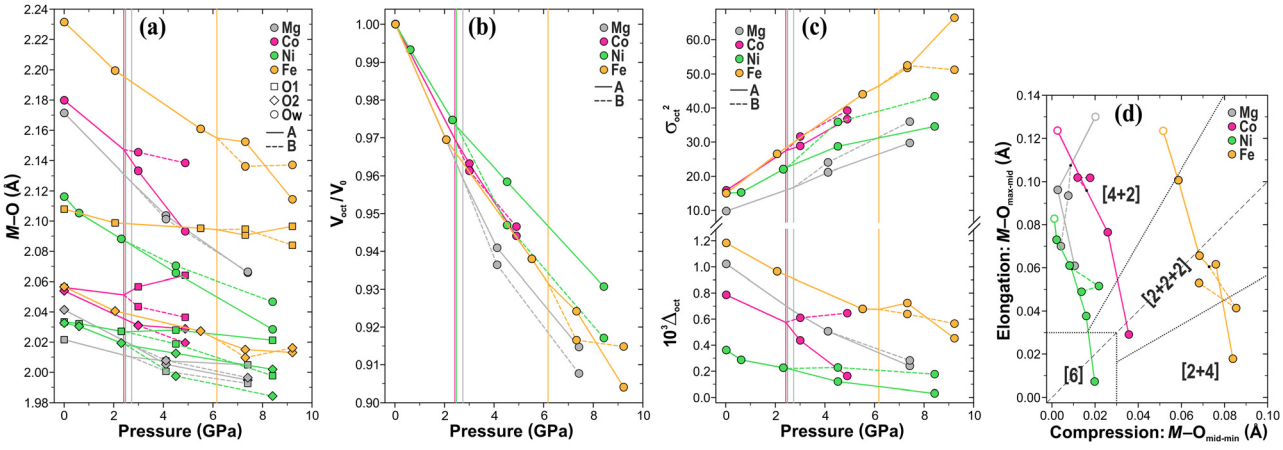

Figure 4: Variation of the octahedral geometries in $MSO_4 \cdot H_2O$ compounds (with *M* = Mg, Fe, Co, Ni) within their *in-situ*-investigated pressure range, as reported in [16–18] and the present work. (a) Individual *M*–O bond lengths; (b) relative octahedral volumes; (c) octahedral distortion parameters Δ_{oct} (distances) and σ_{oct}^2 (angles); (d) style of the octahedral distortion in terms of elongation versus compression. In (a–c) the critical pressures P_c of the $C2/c$ to $P\bar{1}$ phase transitions are indicated by vertical lines, in (d) by a black dot and the 10^{-4} GPa points by open circles. Values at P_c are interpolated from the bracketing data points in the α- and β-phase. For errors see the underlying structural data in [16–18] and Tables 3–5.

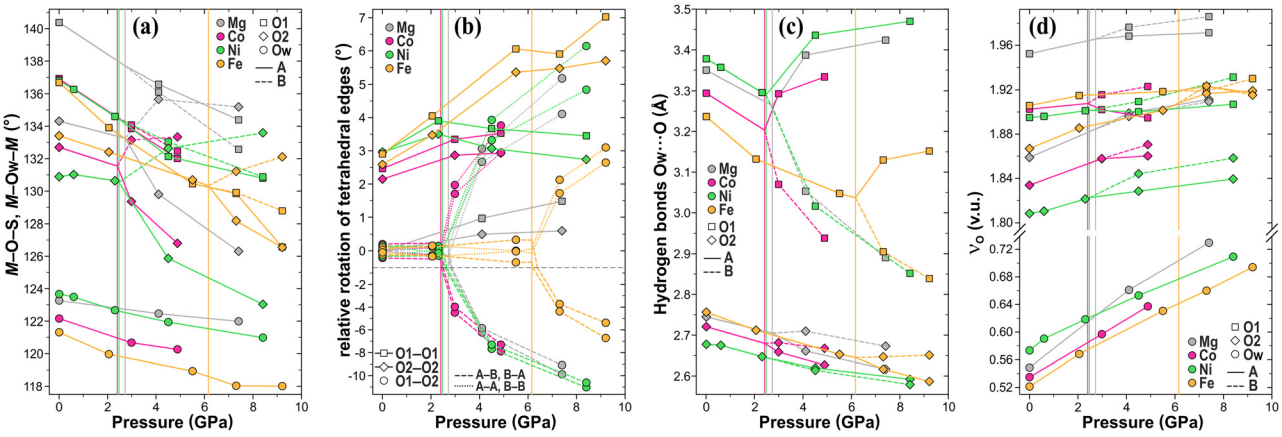

Figure 5: Variation of structure details in $MSO_4{\cdot}H_2O$ compounds (with M = Mg, Fe, Co, Ni) within their *in-situ*-investigated pressure range, as reported in [16–18] and the present work. (a) M–O–S and M–Ow–M angles; (b) rotations of tetrahedral O–O edges (see Figure 3(b)) relative to the α-Mg phase at 10^{-4} GPa; note the different scales (separated by a dashed line) of small/positive rotations versus negative ones; (c) hydrogen bond lengths Ow···O2/O1; (d) bond valence sums for oxygen atoms (without contribution of H atoms). The critical pressures P_c of the $C2/c$ to $P\bar{1}$ phase transitions are indicated by vertical lines. Values at P_c are interpolated from the bracketing data points in the α- and β-phase. For errors see the underlying structural data in [16–18] and Tables 3–5.

the position of the bond critical point $\mathbf{r}_c$ [see 13, and references therein].

On the other hand, Figure 5(b) illustrates that only the loss of the twofold symmetry of the SO_4 tetrahedron at the phase transition allows really substantial tetrahedral rotations especially of the O1–O2 edges, as well as (in part counteracting) edge tiltings, as indicated in Figure 3(b). These edge tiltings are particularly strong and eye-catching in case of the O1A–O1B edge, which in the monoclinic α-phases is forced by symmetry to lie strictly perpendicular to the *b*-axis. In case of the title compound shown in Figure 3, O1A–O1B is tilted by 7.6° at 4.9 GPa, increasing up to 11.5° in the Fe-phase at 9.2 GPa. In our opinion, the symmetry breaking of the SO_4 tetrahedron at the critical pressure is the decisive driving mechanism of the phase transition. The significantly higher P_c in the Fe-compound might then be attributed to the larger and thus more flexible FeO_6 octahedron with its tendency towards a [2+2+2]-coordination already at ambient conditions, which is pursued by the other compounds with increasing pressure (Figure 4(d)).

A further argument to assign the change in the hydrogen bonding scheme, depicted in Figures 3 and 5(c), rather to a side effect than to the driving mechanism of the phase transitions is found in the evolution of the bond valences at the acceptor oxygen atoms with pressure. As Figure 5(d) shows, the 'new' acceptor oxygen O1B exhibits the respective highest bond valence sums of all oxygen atoms in the respective β-phases, i.e. there seems to be no 'need' for O1B to act as acceptor to satisfy its bonding requirements (note that – in order to reduce bias due to the comparatively high uncertainties in the S–O bond lengths – the respective values at 10^{-4} GPa were used at all pressures for the calculation of bond valences according to [41]).

4 Conclusion

The kieserite-type compound α-$CoSO_4{\cdot}H_2O$ undergoes a ferroelastic phase transition at 2.40(3) GPa from a monoclinic $C2/c$ to a triclinic $P\bar{1}$ phase, in analogy to those observed already for the respective compounds of Mg, Fe, and Ni. A further transition to a disordered γ-phase, as detected for $NiSO_4{\cdot}H_2O$, could not be observed within the experimentally accessible pressure range. The most significant structural change under compression is a modification of the hydrogen bonding scheme from two equivalent Ow–H···O2 bonds at ambient conditions to include an additional weaker Ow–H2···O1B bond in the β-phase. This has also been assumed so far as the main driving mechanism of the $C2/c$ to $P\bar{1}$ phase transition. However, the present comparison of topological and crystal chemical data including bond valence calculations suggests that the loss of point symmetry 2 of the sulfate tetrahedra, allowing symmetrically unrestricted tetrahedral rotations and edge tiltings, could be the actual driving mechanism of the phase transition. Moreover, it appears that among the series of isotypic kieserite-type

compounds, specific peculiarities of the Mg-compound (e.g. larger angles at linking oxygen atoms) and Fe-compound (e.g. deviating style of octahedral distortion) are maintained also in their respective high-pressure β-phases.

Author contributions: All the authors have accepted responsibility for the entire content of this submitted manuscript and approved submission.

Research funding: This work was partially supported by a grant from the Austrian Science Fund (FWF): P 29149-N29. Open access was kindly granted by the Open Access Office of the University of Vienna.

Conflict of interest statement: The authors declare no conflicts of interest regarding this article.

References

1. Bishop J. L., Parente M., Weitz C. M., Noe Dobrea E. Z., Roach L. H., Murchie S. L., McGuire P. C., McKeown N. K., Rossi C. M., Brown A. J., Calvin W. M., Milliken R., Mustard J. F. Mineralogy of Juventae Chasma: sulfates in the light-toned mounds, mafic minerals in the bedrock, and hydrated silica and hydroxylated ferric sulfate on the plateau. *J. Geophys. Res.* 2009, *114*, E00D09.
2. Lichtenberg K. A., Arvidson R. E., Morris R. V., Murchie S. L., Bishop J. L., Fernández-Remolar D., Glotch T. D., Dobrea E. N., Mustard J. F., Andrews-Hanna J., Roach L. H. Stratigraphy of hydrated sulfates in the sedimentary deposits of Aram Chaos, Mars. *J. Geophys. Res.* 2010, *115*, E00D17.
3. Mangold N., Gendrin A., Gondet B., LeMouelic S., Quantin C., Ansan V., Bibring J.-P., Langevine Y., Masson P., Nukum G. Spectral and geologic study of the sulfate-rich region of West Candor Chasma, Mars. *Icarus* 2008, *194*, 519–543.
4. Noel A., Bishop J. L., Al-Samir M., Gross C., Flahaut J., McGuire P. C., Weitz C. M., Seelos F., Murchie S. Mineralogy, morphology and stratigraphy of the light-toned interior layered deposits at Juventae Chasma. *Icarus* 2015, *251*, 315–331.
5. Wang A., Jolliff B. L., Liu Y., Connor K. Setting constraints on the nature and origin of the two major hydrous sulfates on Mars: monohydrated and polyhydrated sulfates. *J. Geophys. Res: Planets* 2016, *121*, 678–694.
6. Dalton J. B., Shirley J. H., Kamp L. W. Europa's icy bright plains and dark linea: exogenic and endogenic contributions to composition and surface properties. *J. Geophys. Res.* 2012, *117*, E03003.
7. Kargel J. S. Brine volcanism and the interior structures of asteroids and icy satellites. *Icarus* 1991, *94*, 368–390.
8. McCord T. B., Hansen G. B., Matson D. L. Hydrated salt minerals on Europa's surface from the galileo near-infrared mapping spectrometer (NIMS) investigation. *J. Geophys. Res.* 1999, *104*, 11827–11851.
9. McCord T. B., Hansen G. B., Hibbits C. A. Hydrated salt minerals on Ganymede's surface: evidence of an ocean below. *Science* 2001, *292*, 1523–1525.
10. Nakamura R., Ohtani E. The high-pressure phase relation of the $MgSO_4$–H_2O system and its implication for the internal structure of Ganymede. *Icarus* 2011, *211*, 648–654.
11. Hawthorne F. C., Groat L. A., Raudsepp M., Ercit T. S. Kieserite, $Mg(SO_4)(H_2O)$, a titanite-group mineral. *N. Jb. Min. Abh.* 1987, *157*, 121–132.
12. Wildner M., Giester G. The crystal structures of kieserite-type compounds. I. Crystal structures of $Me(II)SO_4 \cdot H_2O$ [Me=Mn, Fe, Co, Ni, Zn]. *N. Jb. Min. Mh.* 1991, 296–306.
13. Bechtold A., Wildner M. Crystal chemistry of the kieserite-cobaltkieserite solid solution, $Mg_{1-x}Co_x(SO_4) \cdot H_2O$: well-behaved oddities. *Eur. J. Mineral.* 2016, *28*, 43–52.
14. Talla D., Wildner M. Investigation of the kieserite–szomolnokite solid solution series, $(Mg,Fe)SO_4 \cdot H_2O$, with relevance to Mars: crystal chemistry, FTIR, and Raman spectroscopy under ambient and Martian temperature conditions. *Am. Mineral.* 2019, *104*, 1732–1749.
15. Talla D., Balla M., Aicher C., Lengauer C. L., Wildner M. Structural and spectroscopic study of the kieserite-dwornikite solid solution series, $(Mg,Ni)SO_4 \cdot H_2O$, at ambient and low temperatures, with cosmochemical implications for icy moons and Mars. *Am. Mineral.* 2020, *105*, 1472–1489.
16. Meusburger J. M., Ende M., Talla D., Wildner M., Miletich R. Transformation mechanism of the pressure-induced *C*2/*c*-to-*P*1 transition in ferrous sulfate monohydrate single crystals. *J. Solid State Chem.* 2019, *277*, 240–252.
17. Meusburger J. M., Ende M., Matzinger P., Talla D., Miletich R., Wildner M. Polymorphism of Mg-monohydrate sulfate kieserite under pressure and its occurrence on giant icy jovian satellites. *Icarus* 2020, *336*, 113459.
18. Ende M., Kirkkala T., Loitzenbauer M., Talla D., Wildner M., Miletich R. High-pressure behavior of nickel sulfate monohydrate: isothermal compressibility, structural polymorphism, and transition pathway. *Inorg. Chem.* 2020, *59*, 6255–6266.
19. Perez T., Finkelstein G. J., Pardo O., Solomatova N. V., Jackson J. M. A Synchrotron Mössbauer spectroscopy study of a hydrated iron-sulfate at high pressures. *Minerals* 2020, *10*, 1–11.
20. Van Alboom A., De Resende V. G., De Grave E., Gómez J. A. M. Hyperfine interactions in szomolnokite ($FeSO_4 \cdot H_2O$). *J. Mol. Struct.* 2009, *924–926*, 448–456.
21. Miletich R., Allan D. R., Kuhs W. F. High-pressure single-crystal techniques. *Rev. Mineral. Geochem.* 2000, *41*, 445–519.
22. Boehler R., De Hantsetters K. New anvil designs in diamond cells. *High Pres. Res.* 2004, *24*, 391–396.
23. Scheidl K. S., Kurnosov A., Trots D. M., Boffa Ballaran T., Angel R. J., Miletich R. Extending the single-crystal quartz pressure gauge up to hydrostatic pressure of 19 GPa. *J. Appl. Crystallogr.* 2016, *49*, 2129–2137.
24. Jacobson S. D., Holl C. M., Adams K. A. Compression of single-crystal magnesium oxide to 118 GPa and a ruby pressure gauge for helium pressure media. *Am. Mineral.* 2008, *93*, 1823–1828.
25. Angel R. J., Finger L. W. SINGLE: a program to control single-crystal diffractometers. *J. Appl. Crystallogr.* 2011, *44*, 247–251.
26. King H. E., Finger L. W. Diffracted beam crystal centering and its application to high-pressure crystallography. *J. Appl. Crystallogr.* 1979, *12*, 374–378.
27. Gonzalez-Platas J., Alvaro M., Nestola F., Angel R. EosFit7-GUI: a new graphical user interface for equation of state calculations, analyses and teaching. *J. Appl. Crystallogr.* 2016, *49*, 1377–1382.

28. Angel R. J., Gonzalez-Platas J. ABSORB-7 and ABSORB-GUI for single-crystal absorption corrections. *J. Appl. Crystallogr.* 2013, *46*, 252–254.
29. Prince E. *International Tables for Crystallography Volume C*, 3rd ed.; Kluwer Academic Publishers, 2004.
30. Sheldrick G. M. Crystal structure refinement with SHELXL. *Acta Crystallogr.* 2015, *C71*, 3–8.
31. Hübschle C. B., Sheldrick G. M., Dittrich B. ShelXle: a Qt graphical user interface for SHELXL. *J. Appl. Crystallogr.* 2011, *44*, 1281–1284.
32. Birch F. Finite elastic strain of cubic crystals. *Phys. Rev.* 1947, *71*, 809–824.
33. Anderson D. L., Anderson O. L. The bulk modulus-volume relationship for oxides. *J. Geophys. Res.* 1970, *75*, 3494–3500.
34. Chiari G., Ferraris G. The water molecule in crystalline hydrates studied by neutron diffraction. *Acta Crystallogr.* 1982, *B38*, 2331–2341.
35. Shannon R. D. Revised effective ionic radii and systematic studies of interatomic distances in halides and chalcogenides. *Acta Crystallogr.* 1976, *A32*, 751–767.
36. Hazen R. M., Downs R. T., Prewitt C. T. Principles of comparative crystal chemistry. In *High-Temperature and High-Pressure Crystal Chemistry*; Hazen R. M., Downs R. T., Eds.; *Mineralogical Society of America: Rev. Min. Geochem.*, Vol. *41*, 2000; pp. 2–33.
37. Baur W. H. Interatomic distance predictions for computer simulation of crystal structures. In *Structure and Bonding in Crystals*; O'Keeffe M., Navrotsky A., Eds.; Academic Press: New York, II*, 1981; pp. 31–52*.
38. Nazzareni S., Comodi P., Hanfland M. High-pressure single-crystal synchrotron X-ray diffraction of kainite ($KMg(SO_4)$ Cl $3H_2O$). *Phys. Chem. Miner.* 2018, *45*, 727–743.
39. Comodi P., Nazzareni S., Zanazzi P. F., Speziale S. High-pressure behavior of gypsum: a single-crystal X-ray study. *Am. Mineral.* 2008, *93*, 1530–1537.
40. Comodi P., Nazzareni S., Balić-Žunić T., Zucchini A., Hanfland M. The high-pressure behavior of bloedite: a synchrotron single-crystal X-ray diffraction study. *Am. Mineral.* 2014, *99*, 511–518.
41. Brese N. E., O'Keeffe M. Bond-valence parameters for solids. *Acta Crystallogr.* 1991, *B47*, 192–197.